Additive Manufacturing 55 (2022) 102827

Contents lists available at ScienceDirect

Additive Manufacturing

journal homepage: www.elsevier.com/locate/addma

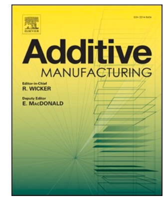

Research paper

From impact to solidification in drop-on-demand metal additive manufacturing using MetalJet

Negar Gilani [*], Nesma T. Aboulkhair, Marco Simonelli, Mark East, Ian A. Ashcroft, Richard J. M. Hague

Centre for Additive Manufacturing, Faculty of Engineering, University of Nottingham, Nottingham NG8 1BB, UK

ARTICLE INFO

Keywords:
Metal additive manufacturing
Metal microdroplet
Metal jetting
Spreading and solidification
Diffusion bonding

ABSTRACT

Drop-on-demand metal jetting is a promising additive manufacturing (AM) technology that is gaining interest due to its capability to directly print complex single and multi-material components at high resolutions. It also has key advantages over other metal AM techniques, such as avoiding powder handling and extensive post-processing. In this method, parts are built via spatially controlled deposition of individual molten droplets onto a substrate. Therefore, the success of the process entirely depends on the behaviour of these single droplets from deposition to solidification including their interactions with the substrate, which is scarcely investigated to date. To fill this research gap, the in-house MetalJet platform was used to investigate the spreading and solidification of metallic micro-droplets at low Weber numbers. This was undertaken onto various substrates using a range of jetting and substrate temperatures through an integrated experimental, analytical, and computational approach. This study reports that increasing the substrate temperature enhanced the diffusion between the droplet and substrate, hence improving the bonding. Moreover, ripples forming on a droplet's periphery during solidification disappeared at elevated substrate temperatures, resulting in improved inter-droplet bonding. Furthermore, the significant role of the substrate wettability and thermal properties, which control the droplet's dynamics and solidification behaviour, respectively, is elucidated. This highlights the importance of substrate material selection using this technology. The results presented in this article underpin the optimal process conditions under which the 3D structures produced with this technology can exhibit reliable integrity and consistency. This represents a step forward in the direct metal printing of high resolution functional multi-material components.

1. Introduction

Metal jetting, as an Additive Manufacturing (AM) method, constitutes dispensing individually controlled micro-droplets of molten metal at precise locations. This approach could open new opportunities in the AM of intricate 3D objects, thanks to its advantages over other metal AM techniques. These include higher resolutions, improved surface quality [1], elimination of powder handling and no residual impurities. Importantly, compared with conventional powder bed-fusion processes, metal jetting enables almost entirely waste-less multi-material 3D printing of metal parts. The uniform droplets can be generated using continuous jetting [2] or in a more controlled manner by drop-on-demand (DOD) [3–8]. Metal jetting shows promise for many sectors, such as, printing of electronic circuits, advanced microelectronic components, complex 3D metal components, biotechnologies, and metal 3D printing in space [9], [10].

In metal jetting, objects are built in a repetitive droplet-by-droplet fashion, hence the precision and properties of components are dictated by the behaviour of the individual droplets (droplet-substrate and droplet-droplet interactions). Due to the independent nature of the droplets upon impact until solidification, investigations on this process can be reduced to studying the characteristics of single droplets. These characteristics, including the droplet morphology, crystal structure and bonding to the substrate (or previously deposited droplets), are based on several factors, such as the thermo-physical properties of the feedstock material and substrate, the droplet and substrate temperatures, the size of droplets, the jetting velocity among others. In order to obtain parts with high integrity, these parameters should be optimised. For this purpose, it is essential to acquire fundamental knowledge about the mechanism of the process through a detailed investigation of single droplet deposition in the first instance. Secondly, the deposition of

* Corresponding author.
E-mail address: negar.gilani@nottingham.ac.uk (N. Gilani).

https://doi.org/10.1016/j.addma.2022.102827
Received 5 February 2022; Received in revised form 8 April 2022; Accepted 12 April 2022
Available online 20 April 2022
2214-8604/© 2022 The Author(s). Published by Elsevier B.V. This is an open access article under the CC BY license (http://creativecommons.org/licenses/by/4.0/).

Nomenclature

D	Droplet's diameter (m)
D_{max}	Maximum droplet diameter (m)
x	Droplet's height (m)
r	Droplet's radius (m)
T_s	Substrate temperature $(^{\circ}C)$
T_D	Droplet temperature $(^{\circ}C)$
T_m	Melting temperature $(^{\circ}C)$
V	Jetting speed (m/s)
θ	Solidification contact angle (°)
k	thermal conductivity $(W/m^{\circ}C)$
c_p	Specific heat capacity $(J/Kg^{\circ}C)$
R_c	Thermal contact resistance (m^2C/W)
L	Latent heat of solidification (KJ/Kg)
R_a	Surface roughness
ρ	Density (Kg/m^3)
σ	Surface tension (N/m)
ϑ	Kinetic viscosity (m^2/s)
μ	Dynamic viscosity $(Pa.s)$
θ	Solidification contact angle (°)
μ	Dynamic viscosity $(Pa.s)$
ϑ	Kinetic viscosity (m^2/s)

multiple droplets, which sets the integrity, should be investigated. Seemingly simple, the first task is already significantly challenging since several complex phenomena occur simultaneously during the deposition and solidification of liquid metal microdroplets onto a substrate [11]. Phenomena that need to be understood include the droplet's dynamics, reactive wetting, and multiphase and multimode heat transfer.

Many experimental [4,12–14] and integrated numerical-experimental [9,15–19] investigations have studied aspects of the impact, spreading, and solidification of droplets during the transient stages of deformation and oscillation. These numerical models may provide reasonable results for millimetre-sized droplets, but the majority of them fail to predict the dynamics of microdroplets at the contact line. This is due to their inaccuracy in accounting for the wetting dynamics. To overcome this limitation, Sprittles et al. [20] developed a computational framework to explore the impact and spreading of micro-droplets of low We numbers onto solid surfaces of varying wettability, where they modelled dynamic wetting using the interface formation model. However, their model did not account for the heat transfer. Using a different approach, Schiaffino et al. [21] established correlations for the time scales of spreading, oscillation and damping during the deposition of microdroplets at low We numbers through scaling analysis coupled with an experimental approach. In other studies, droplet spreading has been considered a precursor to droplet solidification [22–24], thus the heat transfer solution was solved without the interference of the hydrodynamics problem. Despite their simplicity, these models have some limitations in accurately representing the temperature distribution, mainly for large droplet sizes and due to ignoring the effects of convective flow in the liquid metal.

The primary objective of this research is to provide insight into the spreading, solidification, and interface formation mechanisms during the printing of metallic microdroplets using DoD-MJ (Drop-on-Demand Metal Jetting). Moreover, the jetting and deposition parameters involved in producing consolidated 3D prints are optimised. For this purpose, single Sn microdroplets at low We numbers with various temperatures were deposited onto substrates of various temperatures and materials using the bespoke MetalJet platform. The deposits were characterised to correlate their quality to the printing parameters. In parallel, a finite element (FE) model was used to predict the temperature evolution of the droplets and substrate during solidification and cooling. These simulations allowed the investigation of features of the process beyond the resolution available to experimental analysis. Finally, the time scales of droplets' oscillation and damping were calculated using analytical methods to provide information on the dynamics of droplet spreading.

2. Background

2.1. Droplet spreading mechanism

The four principal phases during the impact and spreading of a metallic microdroplet onto a substrate are schematically presented in Fig. 1. At the early stage of impact, i.e. the kinematic phase, the contact diameter increases with time, regardless of the wettability between the droplet and the substrate. In the spreading stage, the contact line is pushed outward radially, and a rim lamella is formed on the periphery of the contact line (Fig. 1-b). Once the contact line is reached its maximum extent, the surface forces act against further spreading of the droplet, and the contact line starts to recede. Here, the dynamic contact angle (θ_d) is smaller than the equilibrium contact angle (θ_e). It has been shown numerically and experimentally that, as in the kinematic phase, wettability does not play a role in the spreading phase [20,25]. In the first two stages, the liquid motion is dominated by inertia forces. The contact line of the retracted droplet $(\theta_d > \theta_e)$ advances during the relaxation phase, and the dynamic contact angle decreases. During this phase, which usually lasts longer than the previous ones, wettability becomes an influential parameter, and it will be determined if the droplet will continue to recoil and oscillate or rebound. The liquid motion in the droplet decelerates at the wetting phase until a steady contact diameter is obtained. The contact angle is equal to the equilibrium contact angle in the non-reactive wetting, and the steady contact angle in the reactive wetting.

Droplet spreading is controlled by the jetting speed (V), initial diameter (D), density (ρ), dynamic viscosity (μ), surface tension (σ) of the droplet, and the wettability of the substrate, which manifests as the contact angle (θ). These parameters can be organised into dimensionless numbers, of which Weber (We) and Ohnesorge (Oh) are the most important to characterise the spreading dynamics for the low impact speed microdroplet. The We number ($We = \rho V^2 D/\sigma$) determines the driving force for droplet spreading onto the substrate. For We$>$ 1, the spreading is mostly impact-driven, while for We$<$ 1, it is capillary-driven, which means the interfacial forces play the deterministic role in driving the spreading process. On the other hand, the Ohnesorge number ($Oh = \frac{\mu}{\sqrt{\rho\sigma D}}$) determines the resistance force. The resistance force is mostly the viscosity for high Oh numbers (Oh$<<$1), while for lower Oh numbers, it is the inertia [22].

2.2. Droplet solidification mechanism

In a non-isothermal process such as DoD-MJ, the final droplet's morphology is partially determined by the time and location of the contact line arrest, which is controlled by the local solidification at the interface. The droplet contact line can potentially be pinned to the substrate in various spreading phases (Fig. 1 a-d) as a function of the substrate and droplet's superheat temperatures, thereby forming the solidification contact angle. However, the initial substrate temperature does not influence the spreading behaviour at any time before the onset of local solidification [21]. Thenceforth, the droplet's liquid parts continue to oscillate during the progressive solidification, whilst the footprints remain unchanged. The oscillations continue until dampened

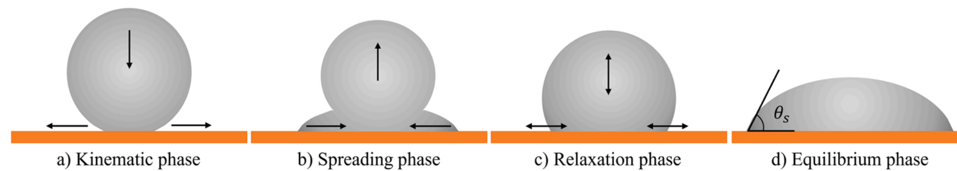

Fig. 1. - Schematic representations of droplet impact and spreading timeline, and dynamic contact angle evolution.

by viscous effects or the droplet is fully solidified.

2.3. Droplet to substrate bonding mechanism

There are three mechanisms of bonding during droplet deposition: physical adsorption, strong metallurgical bonding through melting the substrate, or diffusion of atoms between the substrate and the droplet leading to epitaxial growth or formation of an intermetallic (IM) layer in dissimilar materials. The bonding level in substrate melting is the strongest, hence being more favourable. However, a considerable energy level is required for this type, since the substrate acts as a heat sink because of its significant mass difference to the microdroplets.

3. Materials and methods

The integrated computational, analytical, and experimental approach used in this article is schematically demonstrated in Fig. 2 with detailed descriptions provided in the following sections.

3.1. Experimental methods

The MetalJet [8] platform used in this study to generate and deposit the Sn droplets is schematically presented in Fig. 3. MetalJet adopts Magneto-Hydro-Dynamic (MHD) actuation for droplet generation [26]. In this technique, molten metal is expelled from the orifice in a highly-controlled manner by an electromagnetic force (Lorentz force). The formation and stability of jetting, Acat were continuously monitored by a JetXpert drop watcher (ImageXpert Inc., New Hampshire, USA). A detailed explanation of the MetalJet setup has been described in [3]. In order to minimise the in-flight time and consequent heat loss, the working distance, i.e., the distance between the nozzle and substrate, was set to 1 mm throughout the experiments. Individual Sn droplets with 54.5 µm mean diameter and a standard deviation of 0.5 µm were deposited onto 1 mm thick substrates. The average jetting velocity was measured by JetXpert software, and it was equal to 1.12 m/s. Pure Sn rods (grade 5 N) were used as feedstock material supplied by ESPI Metals.

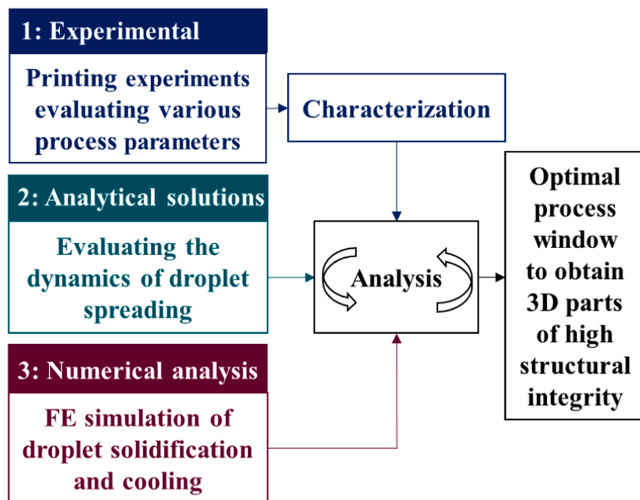

Fig. 2. - The schematic representation of the overall approach used in this study.

Three materials were used as substrates: (1) tempered half-hard OFHC Cu sheets of 99.98% purity, (2) tempered as-rolled Zn sheets of 99.99% purity, and (3) tempered as-rolled Sn sheets of 99.9% purity. These materials were chosen because of their metallurgical compatibility and solubility with liquid Sn. The substrates were polished using SiC papers (grit size 2500) to remove surface oxides and their surface roughness was measured using the optical 3D measurement system Alicona InfiniteFocusG4 (Alicona Imaging GmbH, Graz, Austria). The average height deviation from the mean value, i.e., R_a, was equal to 0.06 µm.

The various parameters used in this study are summarised in Fig. 3, for each combination, 15 droplets were deposited and investigated. The morphology of the droplets, their microstructure, and the droplet-substrate bonding were examined using a FEI Quanta 200 3D Dual Beam FIB-SEM (FEI, Hillsboro, Oregon, USA). Focussed ion beams (FIB) were initially used for cross-sectioning droplet droplets by in-situ stress-free milling. The cross-sections were etched using the ion beam, and lastly, crystallographic orientation contrasts were captured in FIB secondary electron images. Moreover, the equilibrium Sn-Cu phase diagram was obtained using Thermo-Calc software using the TCSLD4 thermodynamic database.

3.2. Finite element model

The 3D thermal model employed in this study was discussed in detail in [3]. The model was generated using a commercial FE package, ABAQUS / standard, version 2019 (Dassault Systèmes Simulia Corp.) to simulate droplet solidification and cooling in the MetalJet process. The droplet geometry and droplet-substrate contact angle were measured from experimental results using an on-screen image measurement software, IC Measure (The Imaging Source Europe GmbH). The thermal model was used to predict the conduction between the droplet and the substrate with general heat convection and radiation on the free surfaces. The temperature distribution throughout the domain satisfies Eq. (1) with the appropriate initial and boundary conditions and temperature-dependent properties.

$$\rho c_p \frac{\partial T}{\partial t} = \frac{\partial}{\partial x}\left(k\frac{\partial T}{\partial x}\right) + \frac{\partial}{\partial y}\left(k\frac{\partial T}{\partial y}\right) + \frac{\partial}{\partial z}\left(k\frac{\partial T}{\partial z}\right) + Q \quad (1)$$

Where c_p is the specific heat capacity and k is the thermal conductivity.

The droplet spreading phase was considered a precursor of the heat transfer process to simplify modelling. However, the effects of convective heat transfer due to the droplet motion were included by using an effective thermal conductivity for the liquid metal, as described in [3]. The temperature-dependent thermal resistance at the interface was also taken into account using the method described earlier [3]. In this approach, the thermal contact resistance depends on the surface roughness and thermal conductivity of the substrate, contact pressure and surface tension of the droplet. The thermo-physical properties of the materials, including density, heat capacity and thermal conductivity, were considered temperature-dependent. A finite temperature range of 2 °C was considered for the solidification of pure Sn (232–230 °C), during which latent heat was 59.5 kJ/kg. The thermophysical properties of Sn, Cu, and Zn ranging from room temperature to 1000 °C are listed in

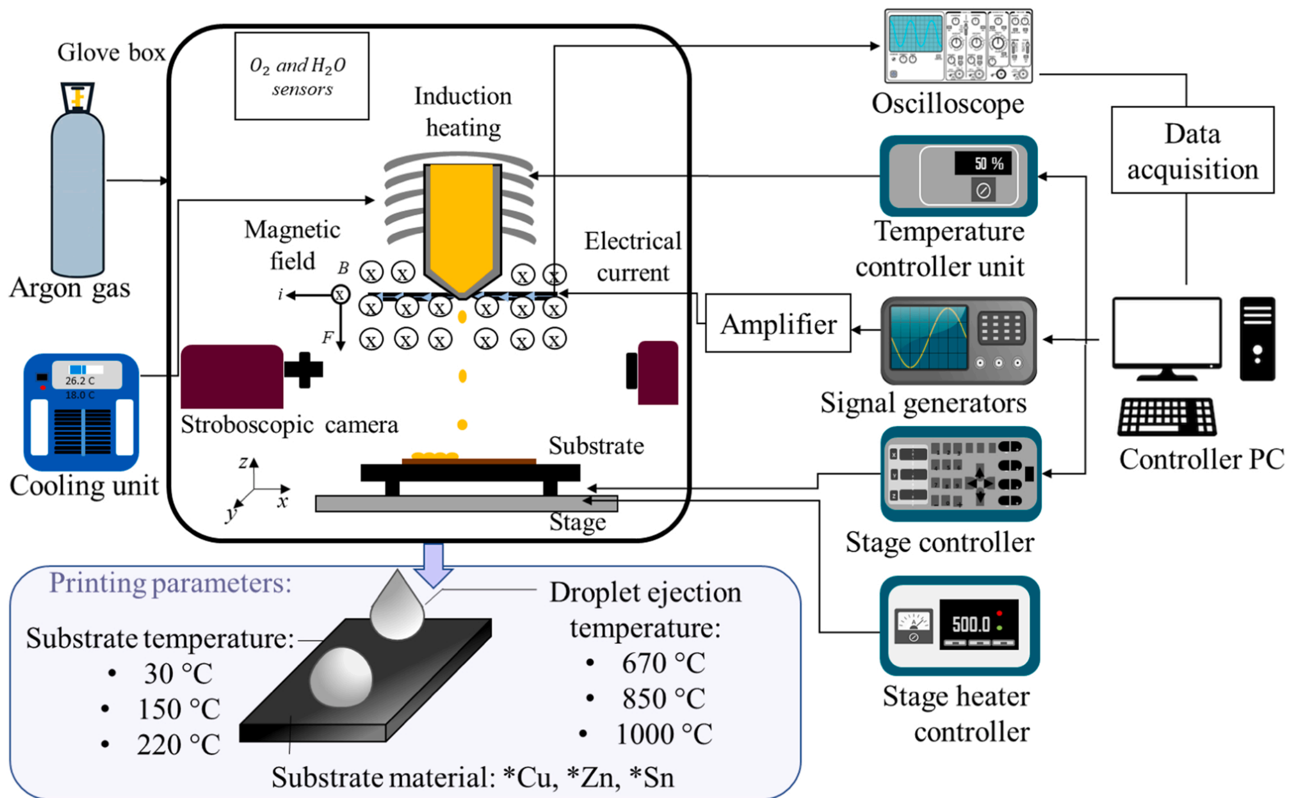

Fig. 3. - Schematic diagram of the MetalJet system and printing parameters used in this study.

Table 1-
Temperature-dependent properties of pure Sn, Cu, and Zn.

Temperature (°C)		27	232	327	1127
Density (kg/m^3)	*Sn*	7300	6900	6850	6300
	Cu	8960	8790	8700	–
	Zn	7130	6980	6900	–
Specific heat capacity (J/kg °C)	*Sn*	207	210.1	211.9	233.5
	Cu	385	408	417	–
	Zn	390	424	444	–
Thermal conductivity (W/m °C)	*Sn*	66.6	56	95.7	163.2
	Cu	401	386	379	–
	Zn	125	114	112	–
Surface tension (N/m)	*Sn*	–	0.546	0.540	0.480
Dynamic viscosity ($Pa.s$)	*Sn*	–	1.8×10^{-3}	1.6×10^{-3}	8×10^{-4}
Kinetic viscosity (m^2/s)	*Sn*	–	2.7×10^{-4}	2.4×10^{-4}	1×10^{-7}

Table 1 [27].

A uniform hexahedral mesh with an element length of 1 µm was used for the droplet. A non-uniform density mesh was used for the substrate, with an element length of 1 µm close to the interface, where the temperature and displacement gradients are the steepest, gradually increasing towards the bottom and sides. Uniform initial temperatures were assigned to both the droplet and substrate. The temperature at the bottom surface of the substrate was kept constant throughout the simulation. Adiabatic conditions were applied to the symmetric surfaces of the droplet and substrate. Heat exchange was enabled at the free surfaces of the droplet and substrate by defining convection and radiation surfaces. A transient heat transfer analysis with a time step of $10^{-9}s$ was used to solve the problem.

4. Results

4.1. Droplet morphology

4.1.1. Effect of superheat temperature

The morphologies of Sn droplets jetted at 670 °C, 850 °C, and 1000 °C to a Cu substrate at 130 °C are shown in Fig. 4 a-c. The droplets' temperatures upon deposition were calculated [8], and they were equal to 651 °C, 822 °C, and 964 °C, respectively. The mushroom shape of the lower temperature droplets changed to an ovoid shape as the droplet temperature increased. At the same time, horizontal solidification ripples were present on the peripheries of droplets for all cases. The temperature evolution of the droplet during impact and solidification is calculated by the FE thermal model (Fig. 4 d) and is compared against the oscillation and damping periods. In this study, We number is in the range of 0.76–0.81, and Oh number is ≅ 0.002. Hence the capillary forces are the main driver for the spreading (We<1), and the inertia is the resistance force (Oh<<1). For such conditions, the oscillation and damping periods are analytically obtained by Eq. (2) and Eq. (3) [21] and the results are demonstrated in (Fig. 4 e):

$$t_{osc} = 2.3 \sqrt{\rho x^3/\sigma} \tag{2}$$

$$t_{damp} = 0.035\frac{x^2}{\vartheta} \tag{3}$$

Where ϑ is the kinetic viscosity and x is the height of the liquid droplet.

After impact, the superheated droplets freely spread on the substrate based on the mechanism explained in Fig. 1. The local solidification at the interface, which arrests the contact line and impedes further spreading, occurred during the relaxation phases (Fig. 1 c). The pinning of the contact line occurs when the droplet's temperature at the interface (shown with dashed lines in Fig. 4 d) dips below the solidification temperature of Sn. According to the FE numerical simulations, solidification at the interface occurs after only 33 µs from the droplet's impact

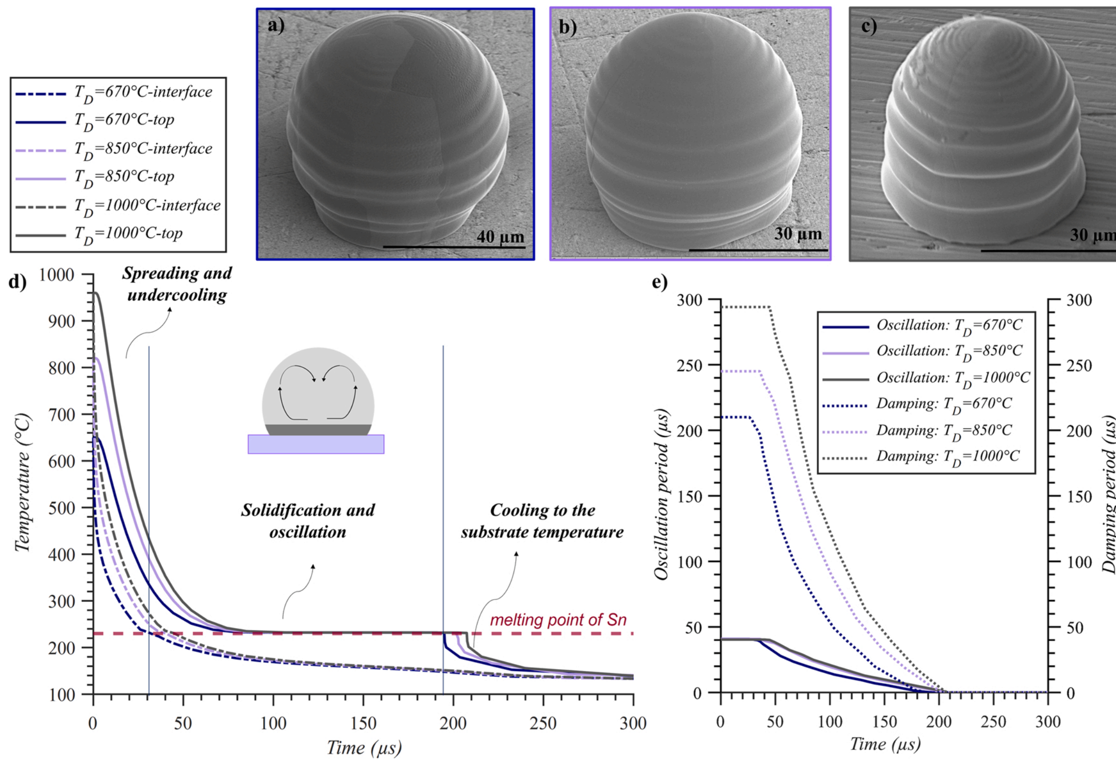

Fig. 4. - Morphology of individual Sn droplets deposited onto a copper substrate at 130 °C, for droplet ejected at temperatures a) 670 °C, b) 850 °C, c) 1000 °C. d) Cooling curves at the central nodes in the interface and top of the droplets when deposited with various superheat temperatures. **e)** Evolution of oscillation and damping periods for the droplets when deposited with various superheat temperatures.

onto the substrate for an initial droplet temperature of 670 °C. The time before solidification at the interface increases as the initial droplet temperature increases; at 850 °C and 1000 °C, it occurs at 42 µs and 47 µs, respectively. After that, droplets continue to oscillate until they completely solidify, as indicated by the temperature at the top of the droplet in Fig. 4 d. The time for the droplet to completely solidify is longer than the predicted oscillation period for all cases (Fig. 4 e). This prediction is supported by the experimental evidence of ripples on the droplets, which formed when the oscillations were frozen in place. The appearance of ripples also shows that there was not enough time for the oscillations to be damped by the viscous effects prior to droplet solidification. This is consistent with the damping period being longer than the solidification time, as predicted in Fig. 4 e.

The spacings between the ripples at the top section of the droplets are smaller, which is due to the decreasing time of oscillation (Fig. 4 e) and the slower solidification front motion (Fig. 4 d). The oscillation period decreases since the effective (liquid) radius decrease with time. Based on the numerical simulations, the bottom of the droplet, at the interface with the substrate, cools down at the highest rate, while the top of the droplet is the last part to solidify. The interval between frozen ripples is a product of the speed at which the solidification front moves upwards and the oscillation period of the remaining liquid. Since they decrease toward the top of the droplet, the wavelength between ripples is shorter in the experimental observation.

Fig. 5 shows the solidification contact angle for various droplet temperatures, experimentally measured from 15 droplets per condition. This angle corresponds to the dynamic contact angle at which the droplet motion has been frozen by solidification. It was observed that the solidification contact angle decreased as the temperature increased. Depending on the superheat temperature, the solidification likely occurred between the relaxation and wetting phases. For higher droplet temperatures, this process was delayed, which resulted in a smaller solidification angle. In the context of DoD AM, a solidification angle of 90° or less is desired, such that no voids or gaps form between adjacent droplets. Another critical parameter in the droplet deposition is the spreading factor (S_{max}). It is the ratio of the maximum diameter (D_{max}) to the initial diameter of the droplet ($S_{max} = D_{max}/D_0$).

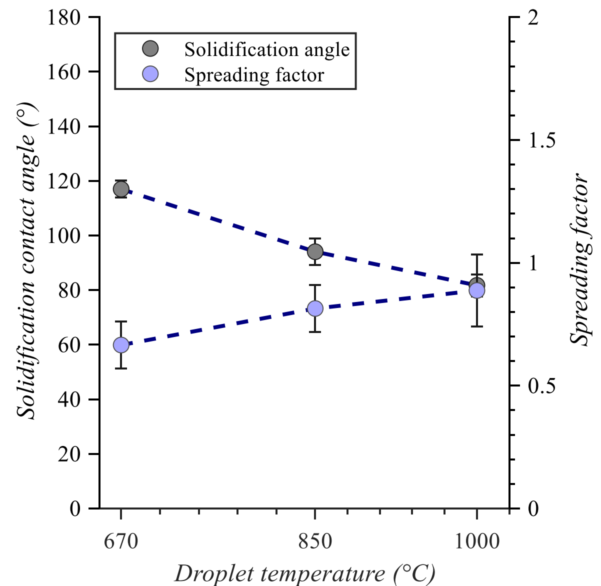

Fig. 5. - The spreading factor and solidification contact angle as a function of initial droplet temperature for substrate at 130 °C. The error bars represent the standard deviation.

The spreading factor is an essential piece of information in droplet-based 3D printing since it defines the required overlap between droplets to build consistent parts. The spreading factor (Fig. 5) was higher for higher droplet temperatures, this is attributed to two main factors.

Firstly, the lower surface tension of Sn at higher temperatures. Secondly and more importantly, the prolonged local solidification at the interface for higher droplet temperatures. As in the wetting phase, the latter allows the droplet to spread further before the contact line is arrested. This also provided more time for a smaller contact angle.

4.1.2. Effect of initial substrate temperature

Three substrate cooling temperatures ($\Delta T = T_m - T_s$), where T_m is the melting temperature of the droplet and T_s is the substrate temperature, were studied. As demonstrated in Fig. 6, the final shape of a droplet with the same initial jetting temperature of 670 °C varies significantly based on the substrate temperature. The temperatures of the droplets were close upon deposition and equal to 647 °C, 651 °C, and 654 °C for substrates at 30 °C, 130 °C, and 220 °C, respectively. At a low substrate temperature (30 °C), concurrently with the outward spreading of the contact line (stage b in Fig. 1), the molten material in the close vicinity of the substrate froze and formed a "solid crust". In this case, the solidification was very rapid (Fig. 6 d) such that the contact line was pinned before further spreading. The molten material in the upper sections pulled back due to the surface tension. Moreover, oscillations in the upper section during solidification left the familiar ripples on the surface of the droplet. With an increase of substrate temperature to 130 °C (Fig. 6 b), the local solidification period increased, which provided time for the droplet to reach the relaxation phase (Fig. 1 c) before the contact line was pinned by solidification. Similar to the droplet with the lower substrate temperature, the molten material in the top section oscillated and solidified in a layer-by-layer fashion from the bottom to the top. At the substrate temperature close to the melting point of the droplet, i.e., 220 °C (Fig. 6 c), the local solidification was sufficiently slow to enable the droplet to enter the wetting stage (Fig. 1 d) before the contact line was pinned due to solidification. It is seen that the influence of the initial substrate temperature on the cooling rate of the droplet is more significant than the initial droplet temperature. The time required for the droplet to completely solidify increased significantly with the substrate temperature from 114 µs to 572 µs, i.e., more than four folds for a temperature increase from 30 °C to 220 °C.

Another important piece of information in Fig. 6 is the evolution of ripples' formation on the surface of the droplets at various substrate temperatures. The evolution of oscillation and damping periods with time for the various substrate temperatures are presented in Fig. 6 e. Even though the solidification speed was lower at higher substrate temperatures (130 °C compared to 30 °C), the ripples on the peripheries were almost alike in Fig. 6 a and b. This can be explained by the longer oscillation period for higher substrate temperatures (Fig. 6 e.), which is indeed a consequence of slower solidification. However, as per Fig. 6 c, the droplet's surface was completely smooth after the solidification of the molten droplets at the elevated substrate temperature. The main reason for such behaviour is that for the 220 °C substrate, the bulk solidification period was longer than the damping period (Fig. 6 d-e); such that the viscosity dampened the oscillations before they froze in place.

The spreading factor and solidification contact angle as a function of the substrate temperature are shown in Fig. 7. The spreading was halted by local freezing very quickly (14 µs) at low substrate temperatures (30 °C). Consequently, a ring lamella was frozen in place, and a large surface area was pinned to the substrate. This accounts for the apparently anomalous results at the lower temperature in Fig. 7. At the intermediate substrate temperature, the surface area was relatively smaller since the local solidification occurred later, allowing the droplet to recoil after the initial spreading phase. Higher substrate temperatures, close to the melting point of Sn, delayed the solidification process such that the droplet had enough time to enter the wetting phase, with increased spreading and decreased contact angle compared with the results at the intermediate temperature.

4.1.3. Effect of substrate material

The side views of individual Sn droplets jetted with an initial temperature of 670 °C onto Cu, Zn, and Sn substrates at 30 °C are presented in Fig. 8 a-c. The droplets were equally cooled in-flight regardless of the

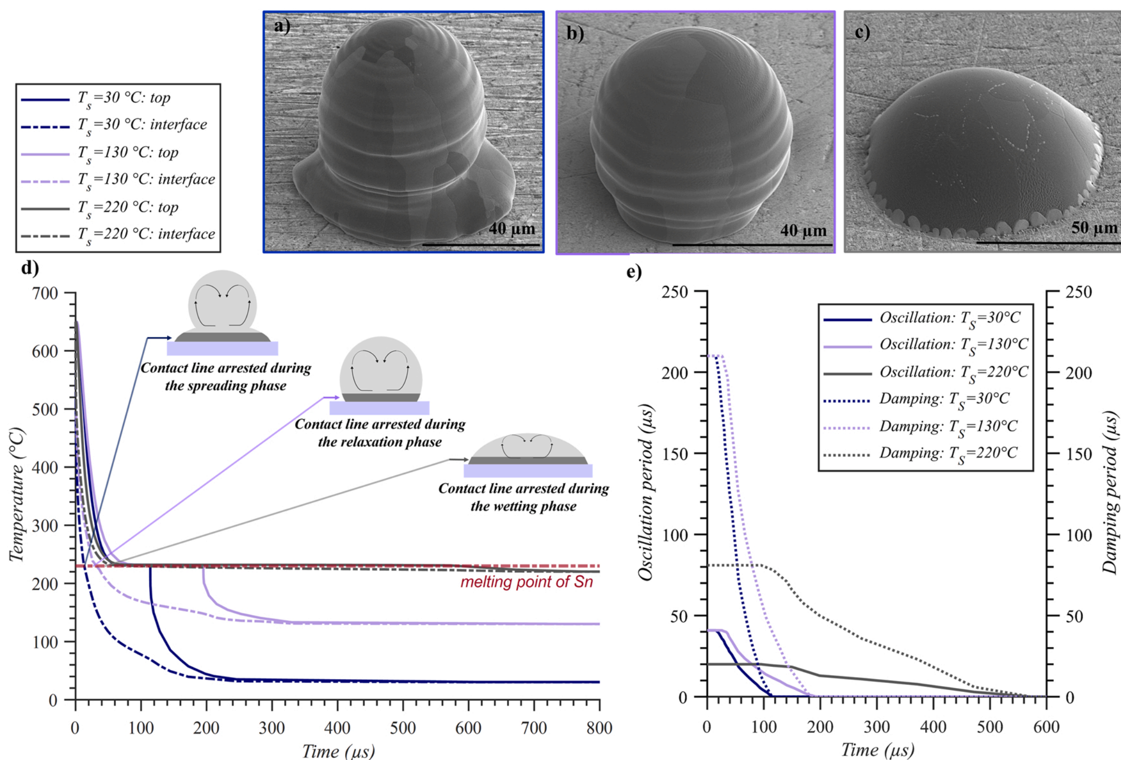

Fig. 6. - Morphology of individual molten Sn droplets at 670 °C onto a Cu substrate with an initial temperature of a) 30 °C, b) 130 °C, and c) 220 °C. d) Cooling curves at the central nodes in the interface and droplet top. e) Evolution of oscillation and damping periods for the droplets when deposited with various substrate cooling temperatures.

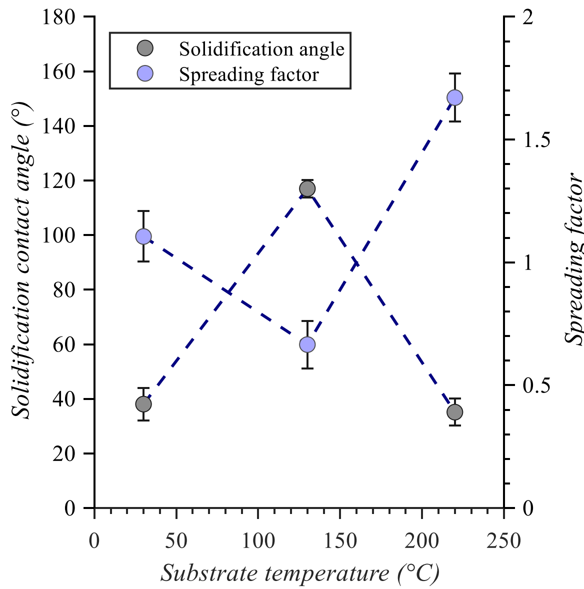

Fig. 7. - The spreading factor and solidification contact angle as a function of initial substrate temperature for droplets jetting at 670 °C. The error bars represent the standard deviation.

substrate material, such that their temperature upon deposition was equal to 647 °C. The influence of the substrate material on the final shape of droplets is more pronounced than that of the substrate or droplet initial temperatures. As shown in Fig. 8 a-b, the contact line of an Sn droplet on an Sn substrate solidified during the relaxation phase instead of the spreading phase for the Cu substrate despite their identical droplet and substrate temperatures. Both substrates are wettable by Sn, however, their dissimilar morphologies upon deposition arise from the different thermal properties of the substrates. Fig. 8 d, demonstrates the notable influence of the substrate thermal properties on the cooling behaviour of droplets. The thermal conductivity of Cu is almost six times higher than Sn at room temperature. Consequently, the local solidification at the interface of a Cu substrate occurs faster (14 μs) than an Sn substrate (71 μs), leading to an altered contact line arrest and, subsequently, different morphologies.

During the experiments, it was observed that most liquid Sn droplets did not adhere to the Zn substrate but were instead bouncing off. The wettability of the substrate by the droplets profoundly influences the deposition behaviour in this regard. If the substrate is not wettable by the droplet, it can lead to a receding break up, which was observed during the deposition of Sn on Zn. Generally, the initial spreading is fast and independent of the substrate's wetting properties. Consequently, it is only during the relaxation phase, where the droplet starts recoiling and oscillating, that de-wetting can potentially occur [20]. It has been proposed that re-bouncing is a violent form of droplet oscillation [28] that happens so fast that droplets bounce off the substrate. Solidification also plays an essential role in a rebound from the substrate. According to the study by Kim et al. [28] regarding the recoil of Sn droplets from a non-wetting surface, the bouncing off phenomenon potentially occurs when the solidification time at the interface is longer than the oscillation period. According to Fig. 8 d and e, the contact line arrests 93 μs after the impact on the Zn substrate, while the initial oscillation period is 54 μs, which explains the re-bouncing of droplets in this case.

Unlike the cases for the other substrates, when depositing on Zn, the droplet's surface was smooth at the top, since the viscosity was able to dampen the liquid oscillations prior to solidification Fig. 8 d-e. The slow solidification is ascribed to the small droplet-substrate contact area due to the poor wetting and the lower heat conductivity of Zn compared to Cu.

The interfacial solidification period for the droplet on the Zn substrate was relatively long, and the droplet likely had enough time to spread fully before it solidified. However, as per Fig. 9, the solidification

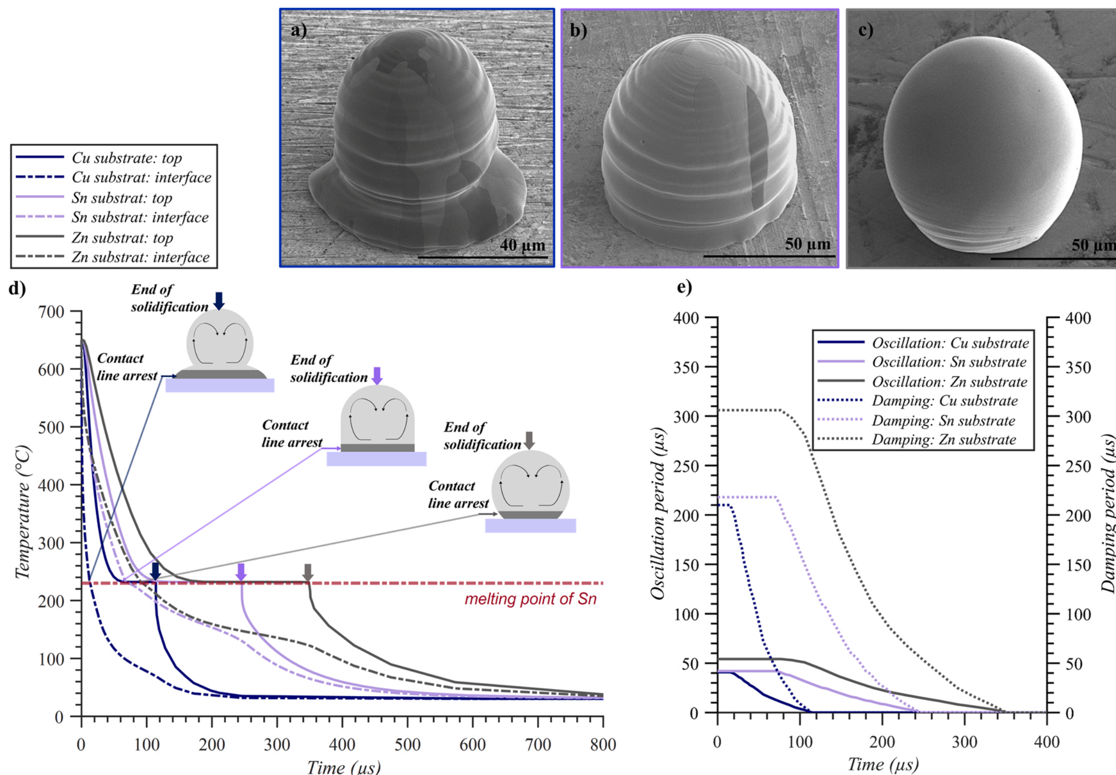

Fig. 8. - Morphology of individual molten Sn droplets at 670 °C deposited onto a) Cu, b) Sn, and c) Zn substrates at 30 °C. d) Cooling curves at the central nodes in the interface and droplet top. e) Evolution of oscillation and damping periods for the droplets when deposited on various substrates.

contact angle was more than 90°, confirming that Zn is not wettable by Sn. The droplet had pinned to the Sn substrate during the wetting phases, also the solidification contact angle was 86° on average, which is greater than the equilibrium contact angle. However, the value being less than 90° proves that the substrate is wettable by the droplet. The spreading factor was lower than the unit value for the Zn substrate since the droplet pulled back due to the poor wettability, while it was more than one for the Sn substrate. The contact angle and spreading factor on the Cu substrate were discussed in 3.2.2.

4.2. Droplet - substrate interface

4.2.1. Effect of superheating temperature

The FIB secondary ion images of cross-sectioned interfaces of Sn droplets jetted at various temperatures onto a Cu substrate at 130 °C in Fig. 11 a-c demonstrate the formation of IM layers at the droplet-substrate interface at all conditions. Two types of intermetallic layers at the interface of liquid Sn and solid Cu are formed [29–32], which is predicted by the Sn-Cu phase diagram and is schematically presented in Fig. 10. Initially, the liquid Sn reacts with the Cu substrate to form a layer of $\eta - Cu_6Sn_5$ as per:

$$6Cu + 5Sn \rightarrow Cu_6Sn_5 \quad (4)$$

Cu atoms diffuse from small grains to larger grains; thus, the initial thin layer transforms to coarsened Cu_6Sn_5 scallops during the ripening process. In the following stage, it is thought that the Cu atoms react with the initial Cu_6Sn_5 layer to form $\epsilon - Cu_3Sn$ (Eq. 4). This reaction is slower since it is solid-state rather than solid-liquid diffusion.

$$Cu_6Sn_5 + 9Cu \rightarrow 5Cu_3Sn \quad (5)$$

The Cu_3Sn grows in time, forming a layer thick enough to impede further diffusion of Cu in the Cu_6Sn_5.

For the droplets deposited at 670 °C, the IM layer (Fig. 11 c) was neither thick nor consistent. The integrity and thickness of this layer improved as the droplet temperature increased (Fig. 11 b-c). Where the average IM layer thickness was 0.29 µm, 0.36 µm, and 0.39 µm with a standard deviation of 0.15 µm, 0.13 µm, and 0.06 µm for 670 °C, 850 °C, and 1000 °C droplets, respectively, hence, improved bonding levels at higher jetting temperatures can be assumed. As per Fig. 11 d, the maximum substrate temperature at the interface is higher at more elevated jetting temperatures. However, the period of time at which these temperatures are maintained lasted less than a hundredth of a microsecond. This explains the negligible variation of IM layer thicknesses since the diffusion varies as a function of time and temperature [32].

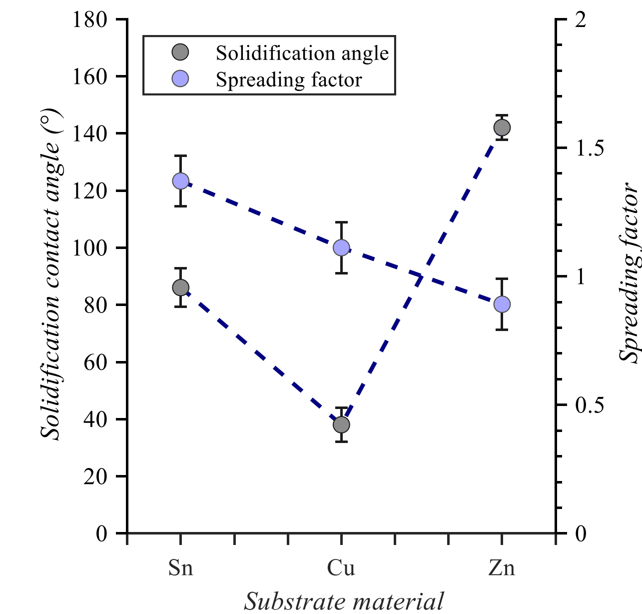

Fig. 9. - The spreading factor and solidification contact angle as a function of the substrate material for droplets jetted at 670 °C onto substrates at 30 °C. The error bars represent the standard deviation.

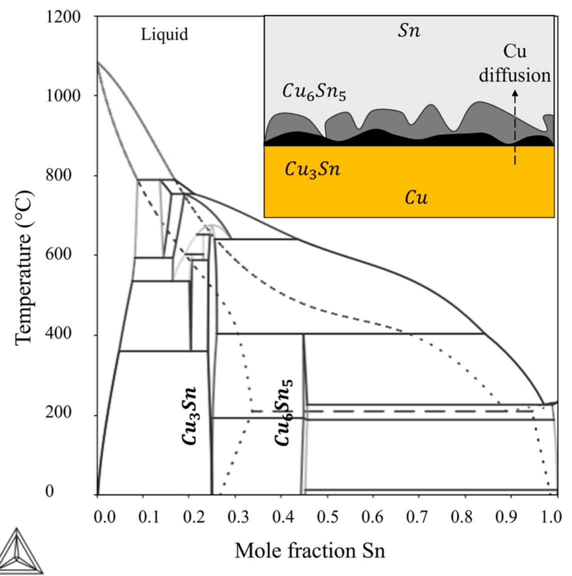

Fig. 10. - Thermo-Calc generated Sn-Cu phase diagram and schematic representation of Cu atom diffusion into liquid Sn to form intermetallic layers.

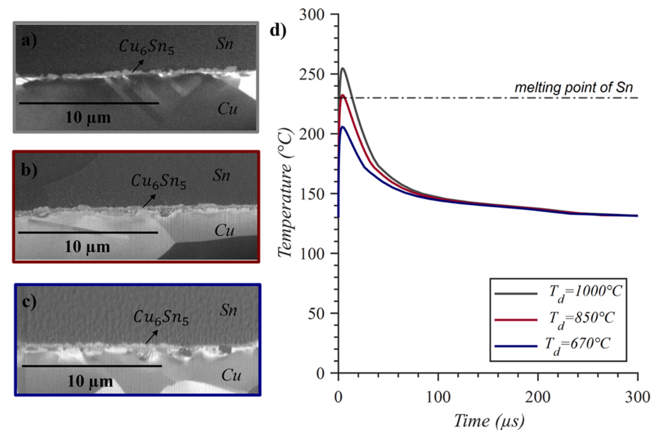

Fig. 11. - FIB-SEM cross-sections of the interfaces for droplets deposited at a) = 1000 °C, b) 850 °C, and c) 670 °C onto a Cu substrate at 130 °C showing the formation of IM layers with various consistency, d) the substrates temperature evolution at the interface during the solidification and cooling of droplets.

4.2.2. Effect of initial substrate temperature

The FIB-SEM cross-sectional views of the interfaces for droplets deposited at 670 °C onto a Cu substrate at various temperatures is demonstrated in Fig. 12 a-c. The temperature at the droplet-substrate interface and the duration at elevated temperature was not sufficient to promote the diffusion of the Cu atoms into the liquid Sn at $T_{substrate} =$ 30°C. As a result, the bonding level was very poor (as evidenced by the droplets peeling off the substrate during handling samples after printing). Increasing the substrate temperature to 130 °C resulted in a thin and non-consistent IM layer at the interface of 0.29 µm on average. At more elevated temperatures, close to the melting point of Sn, the IM layer grew to 1.8 µm on average (with a standard deviation of 0.32 µm) through coarsening of the Cu_6Sn_5 scallops. Moreover, a layer of Cu_3Sn

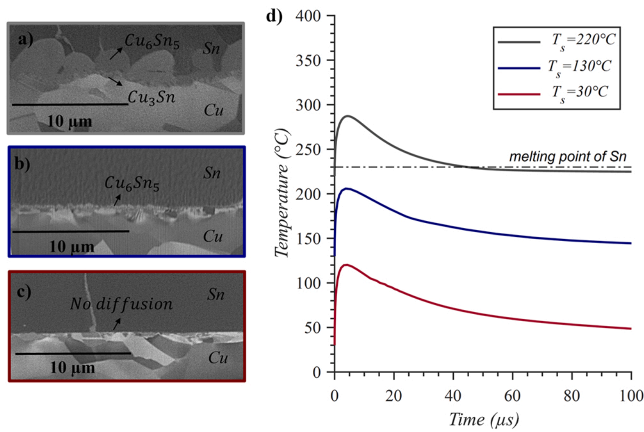

Fig. 12. - FIB-SEM cross-sections of the interfaces for droplets deposited at 670 °C onto a Cu substrate at **a)** 220 °C, **b)** 130 °C, and **c)** 30 °C, showing the formation of IM layers with various thicknesses, d), the substrates temperature evolution at the interface during the solidification and cooling of droplets.

(0.39 µm) formed due to there being sufficient temperature and time for this reaction. This would be expected to increase the strength of bonding at the interface. The temperature evolution at the interface in Fig. 12 d demonstrates that the maximum temperature obtained for substrate at elevated temperature is 287 °C against 120 °C for the substrate at room temperature. Once the steady temperature, i.e., the temperature at which the substrate was kept, was obtained, the diffusion process continued with a higher rate for higher substrate temperature. Moreover, cooling of the substrates from elevated to room temperature extended the diffusion time in these cases.

4.2.3. Effect of substrate material

The FIB-SEM cross-sections of the interfaces for Sn droplets at 670 °C deposited onto substrates of various materials at 30 °C are shown in Fig. 13 a-c. As previously explained (Section 4.2.2), Cu atoms did not diffuse significantly into the liquid Sn droplets due to the low interfacial temperatures. However, a superheated Sn droplet may be expected to form a strong bond to an Sn substrate through substrate melting. However, the droplet and substrate are not fused (Fig. 13 c), and the separation at the interface is clearly visible (white line), which indicates the absence of substrate melting. From the numerical simulations, the interfacial temperature reaches the highest value of 228 °C for the Sn substrate at the droplet centre (Fig. 13 d), which is below the melting point of Sn. Hence a strong metallurgical bonding through melting cannot be expected. The low interfacial temperature is attributed to the thermal resistivity, which in turn is related to the surface roughness. As for the Zn substrate, no diffusion was observed despite the high diffusion rate of Zn atoms into the liquid Sn, which is higher than the inter-diffusion rate of Sn itself or Cu diffusion rate. According to simulation results, the Zn substrate is heated only to 140 °C during the droplet deposition, which is assumed not to be high enough to promote bonding through diffusion (similar to Cu substrate, which was only heated to 120 °C). The lower substrate temperatures reached by the Cu and Zn are attributed to their higher heat capacity compared to Sn. Consequently, no diffusion or melting is expected, as the melting point of Zn is 419.5 °C. As observed experimentally, the droplets only weakly adhered to the Zn and Cu substrates through what can be attributed to van der Waals forces (physical adsorption).

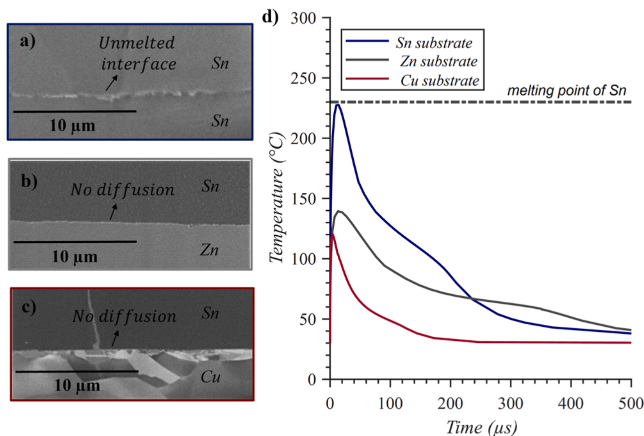

Fig. 13. - FIB-SEM cross-sections of the interfaces for droplets deposited at 670 °C onto **a)** Sn, **b)** Zn, and **c)** Cu substrates at 30 °C, **d)** the substrates temperature evolution at the interface during the solidification and cooling of droplets.

5. Discussion

Metal jetting enables direct and digital manufacturing of complex structures, with the aim of eliminating extensive thermal or surface post-printing treatments required in other AM techniques. In order to obtain structures of high integrity and consolidation without the need for post-pressing, it is essential to fully understand the role of various process parameters involved in this technology to effectively optimise them. In this article, this objective was attained through an in-depth study of single droplets' morphology and their bonding to various substrates. Predicting the final shape of the droplet and understanding the factors that control it are essential for several reasons.

(I) The maximum droplet spreading defines the optimal spacing between the droplets such that there is neither a gap between droplets nor staircasing (Fig. 14 a-b). In this study, the spreading factor increased for higher droplet temperatures, which is in agreement with results previously reported in the literature [21,33]. Here, with a 49% increase in the droplet temperature, the spreading factor was increased by 33% (Fig. 5). The increase of spreading factor as a function of the substrate temperature supports findings in other studies [12,13,17]. However, the theoretical models used in these studies did not match our experimental observations due to the reactive nature of wetting in our research, which influences both the maximum spreading factor and solidification contact angle. It was also seen that by increasing the substrate temperature by 69%, the spreading factor was increased by 149% (Fig. 7). Therefore, our results evidence the more influential role of the substrate's temperature in defining the spreading factor compared to the droplet's temperature.

(II) Inter-droplet voids, which in turn lead to lower relative densities, potentially form if the solidification contact angle is > 90°, as demonstrated in Fig. 14 **c**. High solidification contact angles were observed when substrates were not wettable by the droplets (Fig. 8 **c)**, also when the solidification halted the contact line during the early stages of the relaxation phase (Fig. 6 b). The resultant porosity formation due to these reasons during the deposition of millimetre-sized droplets of pure Al [9, 19] and microdroplets of Ag [8] has been reported in the literature. Moreover, higher solidification contact angles, i.e., lower spreading factors, generate higher surface roughness, which is detrimental for the bonding and deposition accuracy of the next layer of droplets. On the other hand, the precision of the printed part decreases for droplets with a high spreading factor, as shown in Fig. 14 d. The droplet to substrate temperature ratio and substrate material should be carefully chosen to avoid such inter-droplet gaps and poor surface quality.

(III) Molten droplets can unlikely fill the areas between the ripples on the peripheries of previously deposited droplets (Fig. 14 e), creating voids and increasing the thermal resistance at the droplets' interfaces. It was demonstrated that long solidification periods prevent the formation of such striations. High substrate temperatures (Fig. 6 c) or a limited heat transfer between the droplet and substrate (as in the case of the relatively lower thermal conductivity of the Zn substrate) in Fig. 8 c

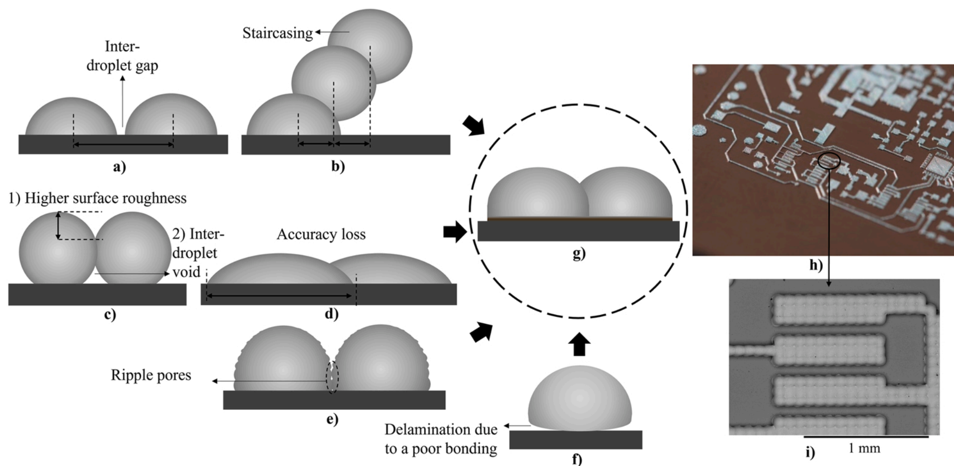

Fig. 14. - **a)** Inter-droplet gap and **b)** droplet staircasing due to overlapping misadjustment, **c)** high surface roughness and inter-droplet void due to high solidification contact angle, **d)** loss of accuracy due to over-spreading of droplets, **e)** pores due to lack of fusion formed at mating surfaces when ripples are present, **f)** droplet delamination due to the poor droplet-to-substrate bonding, **h)** an electronic circuit printed through the MetalJet platform (Sn droplets on a Cu substrate), **i)** SEM image of the electronic circuit showing the consistency of the printed structure.

provided such conditions. Results reported by Yi et al. [19] suggested that droplets deposited onto substrates with low thermal conductivities had a smoother surface, which are in agreement with our findings. However, the claim that solidification ripples could not be improved by controlling the temperature parameters is refuted by our findings.

In addition, the consistency of parts strongly depends on the droplet-to-substrate bonding. The bonding should be robust enough to withstand the thermal stresses generated during the solidification and cooling processes. Otherwise, droplets may delaminate from the substrate, starting at the edges (Fig. 14 f), as reported for Cu microdroplets deposited onto a Cu substrate [3]. We showed that the superheated Sn microdroplets could not melt the entire length of the interface with the low-temperature Sn substrate to form a strong metallurgical bonding (Fig. 13 c). Similar results were reported for superheated Pt [33] and Cu [3] microdroplets deposited onto substrates of similar materials. This can be explained by the considerable mass difference between the microdroplets and the substrate, where the substrate acts as a heat sink and rapidly absorbs the droplet's thermal energy. Another contributing parameter is the thermal resistance at the droplet-substrate interface due to surface roughness and impurities, which limits the heat exchange between them. Another key finding of this article is that printing on dissimilar materials provides the possibility of diffusion bonding below the melting point of the substrate material, as demonstrated in Fig. 12. For such bonding, the substrate should be wettable to allow spreading of the droplet and possesses a high diffusion coefficient to facilitate the diffusion of atoms to the droplet.

The morphology of an optimal droplet with a desirable solidification contact angle ($<90^\circ$) and spreading factor (~ 1), and an improved inter-droplet bonding level, where the solidification ripples are minimised, is demonstrated in Fig. 14 g. This morphology can be obtained if the process parameters mentioned in this study are accordingly optimised, and consequently, parts with high density and consistency could be obtained. Incorporating the findings of the current study, a demonstrator of a defect-free electronic circuit was successfully printed using the MetalJet platform (Fig. 14 h-i).

6. Conclusions

The interaction between molten Sn microdroplets and Sn, Cu, and Zn substrates under various droplet and substrate temperatures was investigated both numerically and experimentally using a novel printing platform based on the MetalJet technology. The specific outcomes from this research are:

- The droplet and substrate initial temperatures play an essential role in the droplet solidification rate and the contact line arrest, hence setting the droplet morphology. The substrate temperature is more influential since it acts as a heat sink.
- Droplets on a medium temperature substrate were pinned to the substrate during the early stage of the relaxation phase when the contact line was not fully advanced. Consequently, a higher solidification contact angle was obtained, leading to potential inter-droplet voids in the printed parts.
- Ripples forming on a droplet's periphery during solidification disappeared at elevated substrate temperatures, resulting in better inter-droplet bonding. The high substrate temperature induces long solidification periods, such that the viscosity effects damp the oscillations before they freeze in place.
- The substrate material is the most influential element in setting the droplets' morphology since its wetting and thermal properties are critical to the droplets' dynamics and solidification, respectively. The Sn droplets wetted the Cu and Sn substrates, whereas the Zn substrate demonstrated poor wettability, leading to potential droplet rebound upon impact, making it impossible to print a consistent part onto a Zn substrate.
- A robust metallurgical bonding through substrate melting was not realised for superheated Sn droplets deposited onto room temperature Sn, Cu and Zn substrates. The reason is that substrates quickly absorb the thermal energy of the microdroplets without a significant increase in the interface's temperature.
- One of the noteworthy outcomes of this research was demonstrating a strong adhesion of droplets to the substrate at temperatures considerably below the melting point of the substrate's material through diffusion bonding, as in the case of Sn droplets deposited onto a Cu substrate.

In conclusion, this research has shown the major role of droplets' morphology and droplet-substrate bonding in the context of drop-on-demand metal additive manufacturing. The findings provide an insight into the effects of various printing process parameters on both aspects. The applicability of knowledge obtained by this study was demonstrated through the successful printing of a defect-free electronic circuit.

CRediT authorship contribution statement

Marco Simonelli: Writing – review & editing, Supervision. **Nesma T. Aboulkhair:** Writing – review & editing, Supervision, Investigation, Funding acquisition. **Negar Gilani:** Writing – original draft, Methodology, Investigation, Formal analysis, Conceptualization. **Richard J. M. Hague:** Writing – review & editing, Supervision, Funding acquisition, Conceptualization. **Ian A. Ashcroft:** Writing – review & editing, Supervision. **Mark East:** Resources.

Declaration of Competing Interest

The authors declare that they have no known competing financial interests or personal relationships that could have appeared to influence the work reported in this paper.

Acknowledgement

The authors are grateful to the Engineering and Physical Sciences Research Council, UK (EPSRC) for funding the MetalJet printing activity through grant reference (EP/P031684/1). The authors are also grateful for the funding provided by the University of Nottingham's Anne McLaren Fellowship and Nottingham Research Fellowship. The authors would like to thank colleagues at Canon Production Printing, Venlo, The Netherlands, for ongoing technical support with regards to the printing platform. Thanks to Dr Christopher Parmenter for training on FIB-SEM and the Nanoscale and Microscale Research Centre (nmRC) at the University of Nottingham for providing access to instrumentation.

References

[1] H. Yi, L. Qi, J. Luo, D. Zhang, N. Li, Direct fabrication of metal tubes with high-quality inner surfaces via droplet deposition over soluble cores, J. Mater. Process. Technol. 264 (2019) 145–154, https://doi.org/10.1016/J.JMATPROTEC.2018.09.004.

[2] M. Orme, Q. Liu, R. Smith, Molten Aluminum Micro-Droplet Formation and Deposition for Advanced Manufacturing Applications 2000.

[3] N. Gilani, N.T. Aboulkhair, M. Simonelli, M. East, I. Ashcroft, R.J.M. Hague, Insights into drop-on-demand metal additive manufacturing through an integrated experimental and computational study, Addit. Manuf. (2021), 102402, https://doi.org/10.1016/J.ADDMA.2021.102402.

[4] S. Haferl, D. Poulikakos, Experimental investigation of the transient impact fluid dynamics and solidification of a molten microdroplet pile-up, Int. J. Heat. Mass Transf. vol. 46 (3) (2003) 535–550, https://doi.org/10.1016/S0017-9310(02)00289-2.

[5] S.I. Moqadam, L. Mädler, N. Ellendt, A high temperature drop-on-demand droplet generator for metallic melts, Micromachines 10 (2019), https://doi.org/10.3390/mi10070477.

[6] S. Haferl, D. Poulikakos, Experimental investigation of the transient impact fluid dynamics and solidification of a molten microdroplet pile-up, Int. J. Heat. Mass Transf. 46 (3) (2003) 535–550, https://doi.org/10.1016/S0017-9310(02)00289-2.

[7] V. Sukhotskiy, P. Vishnoi, I.H. Karampelas, S. Vader, Z. Vader, and E.P. Furlani, "Magnetohydrodynamic Drop-on-Demand Liquid Metal Additive Manufacturing: System Overview and Modelling," 2018. doi: 10.11159/ffhmt18.155.

[8] M. Simonelli, et al., Towards digital metal additive manufacturing via high-temperature drop-on-demand jetting, Addit. Manuf. vol. 30 (2019), https://doi.org/10.1016/J.ADDMA.2019.100930.

[9] H. Li, P. Wang, L. Qi, H. Zuo, S. Zhong, X. Hou, 3D numerical simulation of successive deposition of uniform molten Al droplets on a moving substrate and experimental validation, Computat. Mater. Sci. 65 (2012) 291–301, https://doi.org/10.1016/j.commatsci.2012.07.034.

[10] J. Huang, L. Qi, J. Luo, L. Zhao, H. Yi, Suppression of gravity effects on metal droplet deposition manufacturing by an anti-gravity electric field, Int. J. Mach. Tools Manuf. (2019), https://doi.org/10.1016/j.ijmachtools.2019.103474.

[11] R. de Ruiter, P. Colinet, P. Brunet, J.H. Snoeijer, H. Gelderblom, Contact line arrest in solidifying spreading drops, Phys. Rev. Fluids 2 (2017) 43602, https://doi.org/10.1103/PhysRevFluids.2.043602.

[12] M.V. Gielen, R. De Ruiter, R.B.J. Koldeweij, D. Lohse, J.H. Snoeijer, H. Gelderblom, Solidification of liquid metal drops during impact, J. Fluid Mech. 883 (2021) 32, https://doi.org/10.1017/jfm.2019.886.

[13] F. Tavakoli, S.H. Davis, H.P. Kavehpour, Spreading and arrest of a molten liquid on cold substrates, Langmuir 30 (2014) 52, https://doi.org/10.1021/la5017998.

[14] G. Martouzet, L. Jørgensen, Y. Pelet, A.-L. Biance, C. Barentin, Dynamic arrest during the spreading of a yield stress fluid drop, Phys. Rev. Fluids 6 (2021) 44006, https://doi.org/10.1103/PhysRevFluids.6.044006.

[15] A. Gholijani, C. Schlawitschek, T. Gambaryan-Roisman, P. Stephan, Heat transfer during drop impingement onto a hot wall: The influence of wall superheat, impact velocity, and drop diameter, Int. J. Heat. Mass Transf. 153 (2020), 119661, https://doi.org/10.1016/j.ijheatmasstransfer.2020.119661.

[16] A. Kumar, S. Ghosh, B.K. Dhindaw, Simulation of cooling of liquid Al-33 wt% Cu droplet impinging on a metallic substrate and its experimental validation, Acta Mater. 58 (2009) 122–133, https://doi.org/10.1016/j.actamat.2009.08.063.

[17] S.D. Aziz, S. Chandra, Impact, recoil and splashing of molten metal droplets, Int. J. Heat. Mass Transf. 43 (16) (2000) 2841–2857, https://doi.org/10.1016/S0017-9310(99)00350-6.

[18] M. Pasandideh-Fard, R. Bhola, S. Chandra, J. Mostaghimi, Deposition of tin droplets on a steel plate: simulations and experiments, Int. J. Heat. Mass Transf. (1998), https://doi.org/10.1016/S0017-9310(98)00023-4.

[19] H. Yi, L. Qi, J. Luo, D. Zhang, H. Li, X. Hou, Effect of the surface morphology of solidified droplet on remelting between neighboring aluminum droplets, Int. J. Mach. Tools Manuf. 130–131 (August) (2018) 1–11, https://doi.org/10.1016/j.ijmachtools.2018.03.006.

[20] J.E. Sprittles, Y.D. Shikhmurzaev, The dynamics of liquid drops and their interaction with solids of varying wettabilities, Phys. Fluids vol. 24 (2012).

[21] S. Schiaffino, A.A. Sonin, Molten droplet deposition and solidification at low Weber numbers, Phys. Fluids 9 (1997) 3172, https://doi.org/10.1063/1.869434.

[22] R.K. Chin, J.L. Beuth, C.H. Amon, Thermomechanical modeling of molten metal droplet solidification applied to layered manufacturing, Mech. Mater. 24 (4) (1996) 257–271, https://doi.org/10.1016/S0167-6636(96)00037-3.

[23] Q. Xu, V.V. Gupta, E.J. Lavernia, Thermal behavior during droplet-based deposition, Acta Mater. 48 (4) (2000) 835–849, https://doi.org/10.1016/S1359-6454(99)00389-4.

[24] L.J. Zarzalejo, K.S. Schmaltz, C.H. Amon, Molten droplet solidification and substrate remelting in microcasting Part I: numerical modeling and experimental verification, Heat. Mass Transf. 34 (1998) 477–485.

[25] R. Rioboo, M. Marengo, C. Tropea, Time evolution of liquid drop impact onto solid, dry surfaces, Exp. Fluids 33 (2002) 112–124, https://doi.org/10.1007/s00348-002-0431-x.

[26] M.V. Rasa, R. Berkhout, W.P. J. Classens, C.M. Van, H. Genuchten,E.V. Kuznetsov, Device for ejecting droplets of a fluid having high temperature US 2011/0233239 A1, 2013.

[27] S. Sharafat, N. Ghoniem, Summary of Thermo-Physical Properties of Sn, and Compounds of Sn-H, Sn-O, Sn-C, Sn-Li, and Sn-Si 2000.

[28] H.-Y. Kim, J.-P. Cherng, J.-H. Chun, "Recent Progress in Droplet-Based Manufacturing Research," 2002.

[29] S. Annuar, R. Mahmoodian, M. Hamdi, K.N. Tu, Intermetallic compounds in 3D integrated circuits technology: a brief review, in: Science and Technology of Advanced Materials, Vol. 18, Taylor and Francis Ltd, 2017, pp. 693–703, https://doi.org/10.1080/14686996.2017.1364975.

[30] M.O. Vakanas G., N. Moelans, M. Kajihara, W. Zhang, Formation of compounds and Kirkendall vacancy in the Cu-Sn system, Microelectron. Eng. 120 (2014) 133–137, https://doi.org/10.1016/j.mee.2013.09.009.

[31] Y. Yang, H. Lu, C. Yu, Y. Li, Void formation at the interface in Sn/Cu solder joints, Microelectron. Reliab. 51 (12) (2011) 2314–2318, https://doi.org/10.1016/j.microrel.2011.06.026.

[32] J. Feng, C. Hang, Y. Tian, B. Liu, C. Wang, Growth kinetics of Cu 6 Sn 5 intermetallic compound in Cu-liquid Sn interfacial reaction enhanced by electric current, Sci. Rep. 8 (2018) 1775, https://doi.org/10.1038/s41598-018-20100-1.

[33] H. Merrow, J.D. Beroz, K. Zhang, U.P. Muecke, A.J. Hart, Digital metal printing by electrohydrodynamic ejection and in-flight melting of microparticles, Addit. Manuf. 37 (2021), 101703, https://doi.org/10.1016/j.addma.2020.101703.